DOI: 10.1002/((please add manuscript number))
Article type: Communication

Overall Water Splitting Electrocatalysts based on 2D CoNi Metal-Organic Frameworks and Its Derivative

*Mengjie Liu,[a] Weiran Zheng,[a] Sijia Ran,[b] Steven T. Boles,[b] and Lawrence Yoon Suk Lee [a,]**

[a.] Mengjie Liu, Dr. Weiran Zheng, and Dr. Lawrence Yoon Suk Lee
Department of Applied Biology and Chemical Technology, The Hong Kong Polytechnic University, Hung Hom, Kowloon, Hong Kong SAR, China
[b.] Department of Electrical Engineering, The Hong Kong Polytechnic University, Hung Hom, Kowloon, Hong Kong SAR, China
E-mail: lawrence.ys.lee@polyu.edu.hk (L. Y. S. Lee)

Keywords: water splitting, bimetallic MOF, 2D MOF, nanoplate array, electrocatalyst

Abstract: Efficient electrocatalysts composed of non-precious elements are central to the development of overall water-splitting system. Herein, we demonstrate that two-dimensional CoNi-metal-organic framework (CoNi-MOF) arrays grown directly on a Cu substrate is a highly efficient and stable electrocatalyst for oxygen evolution reaction with a low overpotential (265 mV at 10 mA cm^{-2}) in alkaline medium. With the combination of *in situ* conducting atomic force microscopy and two-point conductivity measurements, we reveal the facilitated electron transfer along the *Z*-axis is than the other directions, which can lead to an enhanced catalytic activity. In addition, a simple annealing treatment converts this 2D CoNi-MOF to a hybrid nanoplate array of metallic nitrides on an amorphous carbon network, which catalyzes the hydrogen evolution reaction with a compatible overpotential of 120 mV (at 10 mA cm^{-2}) and excellent stability. The overall water splitting using these 2D CoNi-MOF-based catalysts shows a 99% Faradaic efficiency at 1.64 V, suggesting a promising pathway forward for the commercial realization of complete water splitting systems.

Growing needs for clean and sustainable energy sources have driven the extensive exploration of energy conversion technologies for several decades with some of these possibly leading to significant changes in the energy landscape, including water splitting, fuel cell, and Li/Na-ion batteries.[1-3] In particular, the water-splitting reaction, consisting of hydrogen and oxygen evolution reactions (HER and OER), is regarded as a promising and efficient pathway to meeting the future energy demands in a clean renewable manner.[4-6] Currently, noble metal-based catalysts exhibit the most active performances, for instance, IrO_2 or RuO_2 for OER and Pt for HER.[7,8] However, the limited abundance, high cost, and narrow useable pH ranges hamper their widespread adoption and hence the discovery of competent electrocatalysts based on earth-abundant elements is highly desired. Among various transition metal-based materials, those composed of Co, Ni, and Fe have recently shown potentials with excellent catalytic properties, and great structural stabilities towards electrocatalytic OER and HER.[9-13] Active site availability and electronic conductivity are the key factors for electrocatalysts, which are determined by the surface species, morphology, and composition. Thus, tremendous effort has been put into the rational design of Co-, Ni-, and Fe-based catalysts and material interface to promote the reaction kinetics and improve the catalytic efficiency.[14,15]

Recently, metal-organic frameworks (MOFs) have attracted great attention due to their flexible, porous structures and tuneable properties.[16,17] Direct exposure of metal nodes in the porous bulk structure to reaction environments makes MOFs a suitable catalyst candidate. Studies show that MOFs possess excellent electrocatalytic activities with high stability against chemical corrosion and bubbles' attack.[17-21] In addition, MOFs can serve as a template of porous carbon-metal structures with good structural stability.[22-27] Nevertheless, most MOF-based electrocatalysts show limited efficiencies due to low mass permeability and poor electrical conductivity. In a bulk MOF, the majority of active sites are located inside pores or channels, where the organic linkers may interfere and thus limit the accessibility.[28,29] To circumvent such shortcomings, thin two-dimensional (2D) MOFs have been suggested to achieve much larger specific surface area

with more active metal sites directly exposed to electrolytes.[30-38] Zhao *et al.*[31] reported that the unsaturated metal atoms on the ultrathin MOF surface could serve as the dominating active centers for OER. They also pointed out that the coupling between metal nodes significantly alters the catalytic activity. More recently, 2D MOFs were prepared by a dissolution–crystallization mechanism on the substrates[30] or selective removal of pillar organics from a 3D pillared-layer MOF.[38] Despite the huge potential, the synthesis of catalytically active 2D MOF with precise control of structure is still challenging, and the real active surface information remain unclear. Thus, the structure-activity relationships among morphology, electronic configuration, and catalytic performance of 2D MOFs still need more explorations.

In this work, we report 2D CoNi bimetallic organic frameworks (CoNi-MOFs) directly grown as nanoplate array on a copper foil under hydrothermal conditions. Such CoNi-MOFs (Co:Ni = 1:1) demonstrate highly active OER catalysis, as manifested by a small overpotential of 265 mV at 10 mA cm^{-2} and Tafel slope of 56 mV dec^{-1} in alkaline media. The superior catalytic activity of 2D CoNi-MOFs is correlated to the dominant $(2\bar{2}0)$ facets, which cause the contraction and enhanced conductivity along the *Z*-axis, and hence facilitate the electron transfer from substrate to active catalytic centers. Moreover, annealing the CoNi-MOF in NH_3 atmosphere yields a hybrid nanoplate array of metallic nitrides on amorphous carbon network (CoNiN@C), which exhibit a low overpotential of 120 mV toward HER. Our work provides solid evidence of the structure-activity relationships in bimetallic 2D MOFs, which can enable this material system as a versatile platform for developing an effective and economic catalytic system.

Bimetallic 2D CoNi-MOFs were grown on a copper foil by a simple hydrothermal process, in which various ratios of Co and Ni precursors were mixed with the organic linker (2,6-naphthalene dicarboxylate) to yield different combination of active sites (Co:Ni = 1:0, 2:1, 1:1, 1:2, and 0:1). **Figure S1** compares the scanning electron microscopic (SEM) images of as-

prepared MOFs. Single metallic Co-MOF adopts a petal-like morphology, whereas Ni-MOF shows bulky cubic structures grown from nanoplates. The MOFs containing both Co and Ni tend to form a 2D nanoplate array. With the Co:Ni ratio of 1:1, the thinnest nanoplate array is obtained, and the nanoplates merge to form thicker plates when the Co:Ni ratio changes to 1:2 or 2:1. The morphology of CoNi-MOF is also affected by reaction duration. **Figure S2** shows how the morphology of CoNi(1:1)-MOF evolves from thin nanoplate arrays to thick bulk structures with reaction time (from 0.5 to 10 h). This suggests that the CoNi-MOFs grow *via* a layer-by-layer stacking process.[39] As-prepared CoNi(1:1)-MOF exhibits vertically aligned 2D nanoplates covering the entire Cu foil substrate (**Figure 1a**). To get more structural details, we collected individual nanoplates by sonicated dispersion in water. A typical transmission electron microscopic (TEM) image of the sample (inset in **Figure 1a**) reveals the sharp angles and clear edges of a nanoplate that is *ca*. 400 × 600 nm^2 in size. From the atomic force microscopic image (AFM, **Figure 1b**), an average thickness of 5.3 nm was determined for a nanoplate. The even distribution of Ni and Co in CoNi(1:1)-MOF nanoplate is confirmed by the elemental distribution mapping shown in **Figure 1c**. The energy dispersive spectroscopy (EDS, **Figure S4**) was used to examine the ratio of Co and Ni in MOFs, which was consistent with the precursor ratio used. For example, the Co:Ni ratio of CoNi(1:1)-MOF was found to be 0.93:1.

For comparison, 3D bulk CoNi(1:1)-MOFs were prepared using the same procedure except for the Cu substrate (**Figure S2e)**. **Figure 1d** compares the X-ray diffraction (XRD) patterns of 2D and 3D CoNi(1:1)-MOFs, both of which agree well with previously reported a pattern of $M(C_{12}H_6O_4)(H_2O)_4$ (M = Co, Ni).[30,40] There are, however, substantial differences in their relative peak intensities between 2D and 3D samples. The (010) peak at 8.7° is dominant in 3D MOF but relatively weak in 2D MOF. On the contrary, the minor (110) and $(2\bar{2}0)$ peaks in the 3D sample appear intense in the 2D sample, suggesting that those are two highly exposed facets

in 2D MOF, which is consistent with the SAED pattern in **Figure 1c**. Based on the XRD results, a possible structure is proposed in **Figure 1e**, where one wide plane and two narrow edge planes are composed of $(2\bar{2}0)$ (blue), (010) (red), and (110) facets (green), respectively. The larger surface area in the 2D structure allows more metal sites to be exposed on the surface compared to the 3D counterpart.

The surface species of 2D and 3D samples are studied by X-ray photoelectron spectroscopy (XPS, **Figure 1f**). Both 2D and 3D CoNi(1:1)-MOFs show similar binding energies for Co $2p_{3/2}$ of *ca*. 781.1 eV. However, the binding energy of Ni $2p_{3/2}$ in 2D MOFs (856.30 eV) is 0.35 eV higher than that of a 3D sample (855.95 eV). This slight shift in binding energy is attributed to the more oxidizing environments for surface Ni species due to the surface-absorbed OH radicals. The calculations based on the XPS results also reveal that there are more Ni atoms present on the surface of 2D MOF than 3D MOF. The calculated surface Ni:Co ratios are 1.19 and 1.04 for 2D and 3D MOF, respectively. The selective exposure of $(2\bar{2}0)$ facet by adopting 2D structure affects both the distribution of surface species and the electronic properties of Ni in CoNi-MOF.

We further investigated the effect of Co:Ni ratio on the fine structure of 2D MOFs nanoplates. As shown in **Figure 2a**, all the MOFs with different Co:Ni ratios show the major XRD peaks at similar angles, an indicative of similar structures due to small difference (5.5 pm) in the ionic radii of Co^{2+} and Ni^{2+}. This isostructure was also confirmed by Raman spectra (**Figure S5a**). However, careful analysis of the XRD patterns unveils that two peaks for (110) and $(2\bar{2}0)$ vary with Co:Ni ratio (**Figure 2a**). The smallest *d*-spacing from CoNi(1:1)-MOF indicates the lattice contraction along the *Z* direction (inset in **Figure 2a**). Such structural contraction can induce an increased overlap between metal nodes[41] and may contribute to the enhanced conductivity of MOFs along the *Z*-axis by facilitating the electron transfer towards the edge, thus boosting the OER process on these sites. This is supported by an *in situ* conducting-AFM image of

oblique MOF nanoplates on Cu substrate (**Figure 2b**), where the bright lines visualize the higher current density along the edges. The electric current flow was measured between tip and sample for an applied DC bias (100 mV) by using a conductive probe in the contact mode. The schematics and the corresponding topologic AFM image are presented in **Figure S6**. To further confirm the directional conductivity on the nanoplates of CoNi(1:1)-MOF, we employed the nanomanipulators in a focus ion beam (FIB) microscope for two point-probe measurements (**Figure S7**). Among three directions accessed (*Z*-axis, diagonal, and *X*-axis, inset in **Figure 2c** and **S8**), the contacts along the *Z*-axis exhibit the highest current response upon voltage sweep, which confirms the enhanced conductivity compared to other directions.

The electrochemical surface area was measured by cyclic voltammetry from 1.15 to 1.20 V (**Figure S9**), and the plots are shown in **Figure 2d** with the calculated areal capacities. Ni-MOFs exhibit areal capacities of merely 6 mF cm^{-2}. The areal capacitance increases with the incorporated Co contents, and the highest value was obtained with CoNi(1:1)-MOF (245 mF cm^{-2}), which is consistent with SEM and AFM results of the thinnest nanoplates. Further increase in the Co ratio lowers the areal capacitance, probably due to the transition to 3D MOF, forming thicker nanoplates. Thus, by introducing Co and Ni with 1:1 ratio, 2D nanoplate MOFs with the high surface area and exposed $(2\bar{2}0)$ facets can be achieved. The XPS results of 2D CoNi-MOFs with different Co:Ni ratios (**Figure S10**) show that their surface Co and Ni species are of similar chemical states as in CoNi(1:1)-MOF.

With different morphological and structural features, as-prepared MOFs were tested for OER catalytic activities using a standard three-electrode cell in 1 M KOH (see the SI for experimental details) and the linear polarization curves are shown in **Figure 3a**. Followed by an oxidation peak of surface metal species (M-OH to M-OOH) between 1.20 and 1.50 V, all MOFs show catalytic activities towards OER. A current density of 10 mA cm^{-2} was measured from CoNi(1:1)-MOF at an overpotential of 265 mV, which outperforms the commercial RuO_2 and

most MOF-based catalysts previously reported (**Table S1**). The overpotentials of 301, 309, 341, and 375 mV were required for CoNi(1:2)-MOF, CoNi(2:1)-MOF, Co-MOF, and Ni-MOF, respectively. It is noteworthy that the pre-OER oxidation peak gradually shifts to lower potentials with the amount of Co content, implying the changes in the electronic structure of metal nodes.[6,42] The CoNi(1:1)-MOF shows the smallest Tafel slope of 56 mV dec^{-1}, an indicator of the highest activity among all the samples investigated (**Figure 3b**).

Such high catalytic activity of the Co:Ni(1:1)-MOF partially arises from the large surface area. Electrochemical impendence spectroscopy (EIS) was used to gain more insights into the enhanced catalytic activity. **Figure 3c** shows the Nyquist plots of MOFs at 1.55 V in 1 M KOH. Two half circles are present in all the cases, suggesting two charge transfer processes in MOFs: self-oxidation of metal sites and OER. The fitted charge transfer resistance for OER is 3.745 Ω (Ni-MOF), 2.328 Ω (Co-MOF), 1.038 Ω (CoNi(1:2)-MOF), 1.654 Ω (CoNi(2:1)-MOF), and 0.924 Ω (CoNi(1:1)-MOF). Thus, CoNi(1:1)-MOF possesses the smallest resistance that will contribute to the facilitated catalytic reaction. In general, the presence of two metal sites is known to increase the conductivity higher than either of single metallic MOFs,[30,31,43] as a result of the synergistic effect from two different metal nodes. This enhanced conductivity of CoNi-MOFs, especially CoNi(1:1)-MOF, could be associated with the lattice contraction along the *Z*-axis (**Figure 2a**) which correlates to a reduced metal-to-metal distance. The electrochemical characterizations support that the high activity of CoNi(1:1)-MOF is a combined result of both morphologic (high surface area with more metal sites exposed) and electronic (high conductivity) aspects.

The unique structural features of MOFs also grant the stability during catalysis. We have tested the stability of CoNi(1:1)-MOF during electrolytic OER, and the results are presented in **Figure 3d**. The current density is stable under alkaline environments over 20 h of high current test (28 mA cm^{-2}) with 9.9 % lose (3.3 % loss at 13.5 mA cm^{-2} over 13 h), which confirms that

CoNi(1:1)-MOF is a highly durable electrocatalyst. Post-OER characterization by SEM, TEM, XRD, and XPS show the nanoplate array structure is still retained with oxidized active species formed (**Figure S18**).

The HER is another essential half-reaction of water-splitting. By annealing the CoNi(1:1)-MOF under NH_3 atmosphere, the hybrid nanoplate arrays of Ni nitride composites were prepared on amorphous carbon network (CoNiN@C). **Figure 4a** shows the morphology of CoNiN@C where the 2D nanoplate morphology remains unchanged after annealing treatment. The TEM image of nanoplate (inset of **Figure 4a**) displays the porous surface with an average length of *ca*. 600 nm. The surface is composed of evenly distributed nanoparticles with a mean size of 17 nm in an amorphous carbon matrix (**Figure 4b**). The typical D and G peaks of carbon in Raman spectra confirm the *in situ* incorporated carbon (**Figure S5b**). Under the treatment conditions, Ni_4N nanoparticles are formed as suggested by the clear lattice spacings of 0.216 and 0.187 nm, which can be assigned to the (111) and (200) planes of Ni_4N, respectively (top-left inset in **Figure 4b**). Selected area electron diffraction (SAED) pattern indicates the crystallinity of Ni_4N with the rings corresponding to the (111), (200), (220), and (311) planes (top-right inset in **Figure 4b**). The XRD pattern of CoNiN@C (**Figure S11**) further confirms the existence of Ni_4N, with the diffraction peaks at 41.7°, 48.6°, and 71.2° corresponding to the (111), (200), and (220) lattice planes, respectively.[44,45] Metal nitrides are regarded as a HER active material under basic and neutral conditions, where the adsorption and subsequent dissociation of H_2O are the rate-limiting steps.[46] Both theoretical and experimental studies suggest that metal nitrides facilitate the adsorption and dissociation of H_2O,[47] as well as charge-carrier transfer.[48,49] The low valence metal centres serve as hydride-acceptors, to which the formed OH^- can be easily transferred under the electrostatic effect, facilitating the separation of H_2O.[50] On one hand, N ions accept protons which further react with electrolyte to generate H_2.[46] On the other hand, no Co species is evident from TEM or XRD characterizations, but elemental

distribution mapping suggests even distribution of Co, Ni, N, and C (**Figure S12**). It may be due to the small size or poor crystallinity of particles of highly dispersed Co species.

XPS analysis (**Figure 4c**) reveals the surface elemental states of CoNiN@C. Two peaks at 852.6 and 853.5 eV can be assigned to Ni-N ($Ni^{\delta+}$) and Ni-O (Ni^{2+}) species, respectively.[6, 32] From the Co XPS spectrum, partially oxidized $Co^{\delta+}$ (778.1 eV, $0 \leq \delta < 1$) is evident, which has a strong affinity for hydride intermediate during the HER due to its metallic properties. Other species, such as Co^{2+} (781.0 eV) and Co^{3+}(779.2 eV) can be assigned to Co-O and Co-N bond, respectively.[51] **Figure 4d** compares the linear polarization curves of commercial Pt/C, CoNiN@C, and CoNi(1:1)-MOF towards HER. The CoNiN@C shows an overpotential of 120 mV to achieve 10 mA cm^{-2}, which is better than CoNi(1:1)-MOF (376 mV) and comparable to other reported Ni/Co-based systems (**Table S2**). Such a difference in the activities of CoNi(1:1)-MOF and CoNiN@C can be explained with both structural and electronic aspects. The areal capacitance of CoNiN@C determined by CV is 39.2 mF cm^{-2} (**Figure S13**), much larger than that of CoNi(1:1)-MOF (1.3 mF cm^{-2}). From an electronic perspective, the EIS results shown in **Figure S14a** suggest that CoNi(1:1)-MOF has a much higher charge transfer resistance (102.4 Ω) than CoNiN@C (4.62 Ω). It is concluded that both structural and electronic factors better promote the HER activity on CoNiN@C than CoNi(1:1)-MOF. Long-Term chronoamperometric electrolysis conducted with CoNiN@C at -0.15 V showed that the current density decreased by less than 9 % over 12 h (**Figure S14b**), demonstrating the stable nature of CoNiN@C.

With the promising OER and HER results, we performed an overall water splitting using CoNi(1:1)-MOF and CoNiN@C as the anode and cathode, respectively. Previous results show that the overpotentials of OER and HER are 265 and 120 mV, suggesting the overall potential of *ca*. 1.62 V. With a two-electrode cell, an overpotential of 1.64 V is required to reach 10 mA cm^{-2}. As expected, both electrodes show superior durability under different potential with a

negligible drop in current density (**Figure S15**). To evaluate the Faradaic efficiency, we also compared the measured and calculated amount of H_2 and O_2 (**Figure S16**). The measured gas production agrees well with the calculated value, and the molar ratio of produced H_2 to O_2 under the same current density is about 2:1. The Faradaic efficiency is estimated to be 99.0% for H_2 production on CoNiN@C and 98.9% for O_2 production on CoNi(1:1)-MOF.

We prepared a 2D nanoplate array of CoNi-MOF with $(2\bar{2}0)$ facets exposed. XPS results show that the surface of such 2D MOF is enriched with partially oxidized Ni. By altering the Co:Ni ratio, the lattice contraction along the *Z*-axis ((110) facet) is observed and analysed for the first time. The largest surface area and lowest charge transfer resistance are achieved with an optimized Co:Ni ratio of 1:1. Both structural and electronic features of CoNi(1:1)-MOF contribute to the low overpotential (265 mV at 10 mA cm^{-2}) and high stability towards OER. By annealing CoNi(1:1)-MOF in ammonia atmosphere, porous 2D nanoplate array of CoNiN@C with high areal capacitance was prepared. The existence of Ni_4N nanoparticles was confirmed by HRTEM, XRD, and XPS results. The CoNiN@C shows a comparable overpotential of 120 mV (at 10 mA cm^{-2}) and a significantly lower charge transfer resistance than CoNi(1:1)-MOF. From overall water splitting performed using CoNi(1:1)-MOF and CoNiN@C as an anode and a cathode, respectively, a voltage of 1.64 V was required to reach 10 mA cm^{-2}, and the Faradaic efficiency is calculated to be 99.0% (HER) and 98.9% (OER) after 80 min of water electrolysis.

1. Experiment Section

1.1 Materials synthesis

1.1.1 Preparation of CoNi(1:1)-MOF nanoplate arrays grown on a copper foil

Cu substrate was cut into 3 × 2 cm^2 rectangle and corroded in 5% HCl for 5 min to remove any oxide species on the surface, followed by sonication with ethanol and DI-water for 10 min each. The dried substrate was then vertically inserted into a Teflon ring, making no side facing downwards or upwards. Cobalt acetate tetrahydrate ($Co(Ac)_2 \cdot 4H_2O$, 0.2 mmol) and nickel acetate trihydrate ($Ni(Ac)_2 \cdot 4H_2O$, 0.2 mmol) were mixed into DI water (25 mL) under vigorous stirring for 5 min. Meanwhile, 2,6-naphthalene dicarboxylate acid (NDC, 0.4 mmol) and equal amount of KOH were dissolved separately in DI-water (25 mL) to form a salt solution. Two solutions were mixed with gentle shake to avoid the precipitation at room temperature. The prepared substrate and solution were transferred into an 80 mL Teflon-lined stainless-steel autoclaves, heated to 80 °C for 2 h, then cooled down to room temperature in the water bath for 30 min. The final products on copper foil were repeatedly washed with water for several times and air-dried for 2 h under room temperature. The heating time was changed to 0.5, 1.5, 6, 10, and 20 h to obtain MOFs with different morphologies.

1.1.2 Preparations of bulk CoNi (1:1)-MOF powder

The same synthetic procedure described in the previous section was used without a substrate. The bulk CoNi (1:1)-MOF was collected directly from the autoclave.

1.1.3 Preparations of Co-, Ni-, CoNi(1:2)- and CoNi (2:1)-MOF arrays grown on copper foil

The synthetic procedure described in section 1.1.1 was used, except that the ratio of metal ions was controlled (Co:Ni = 1:0, 0:1, 1:2, and 2:1), maintaining the total amount the same as 0.6 mmol.

1.1.4 Preparation of CoNiN@C porous nanoplate arrays

The CoNi(1:1)-MOFs grown on the copper substrate were used as precursors for carbonization in a tube furnace with a flow of ammonia at a rate of 50 sccm. The temperature was increased from 20 to 400 ℃ with a ramp rate of 5 ℃/min and kept for 2 h before cooling down to room temperature. The final carbon nanoplate arrays were obtained.

1.2 Physical characterization

X-ray diffraction patterns (XRD, SmartLab X-ray diffractometer Rigaku) was measured to analyze the crystal structure of materials. Scanning electron microscopy (SEM) was performed using a JEOL Field Emission SEM. Transmission electron microscopic (TEM) images were taken by a STEM (JEOL JEM-2100F). The elemental compositions analysis and distribution mapping of materials were conducted on an energy dispersive spectrometer (EDS) equipped with the STEM. X-ray photoelectron spectroscopy (XPS) analysis of the material was carried out using a Thermo Fisher ESCALAB 250Xi. The binding energy scale of the spectrometer was calibrated using the position of C 1s peak at 284.6 eV. Raman scattering was performed using a Raman spectrometer (LabRam HR800-UV, Horiba-Jobin Yvon) with 532 nm laser excitation. Atomic force microscopy (AFM) was performed by Brucker multimode8-HR (peak-force tapping mode: SNL-10 cantilever; conducting mode: SCM-PIT-V2 cantilever). Dual beam multi-system focus ion beam (FIB) with two-point probe measurement was taken by a JEOL Model JIB-4501.

1.3 Electrochemical measurements

Both HER and OER tests were performed in a standard three-electrode electrochemical cell and data were collected by the electrochemical stations CHI 760E and PARSTAT 2273 in 1 M KOH at 25℃. The as-synthesized MOFs and CoNiN@C on copper foils with a clamp were directly used as the working electrodes, while a Pt foil for OER (graphite rod for HER) and saturated calomel electrode (SCE) were employed as counter electrode and reference electrode, respectively. All current densities were calculated by the geometrical area of electrodes and measured currents. Before each electrochemical test, the working electrodes were stabilized by 20 cycles of cyclic voltammetry (CV) at 50 mV/s. For OER tests, linear sweep voltammograms (LSV) were obtained from 0.1 to -0.5 V *vs*. RHE at a rate of 5 mV s^{-1}. For HER tests, LSVs

were measured from 1.0 to 1.7 V *vs*. RHE at a rate of 5 mV s^{-1}. The overall water splitting performances were tested in 1 M KOH electrolyte, using CoNi(1:1)-MOF nanoplate arrays as positive electrodes and CoNiN@C nanoplate arrays as negative electrodes.

1.3.1 Calibration of the reference electrode

The potentials were converted to a reversible hydrogen electrode (RHE) based on the following equation: $E_{(RHE)} = E_{(SCE)} + 1.032$ V, where 1.032 V is read from the calibration experiment in a H_2-saturated 1 M KOH solution. In this process, counter electrode and working electrode were both platinum electrodes, and the reference electrode was saturated calomel electrode. CV was measured from -0.9 to -1.1 V at a scan rate of 5 mV s^{-1}. The standard potential of RHE was the average value of anodic and cathodic potential when the current was zero. The CV curves are shown in Fig. S17.

1.3.2 IR compensation

To correct LSV curves, electrochemical impedance spectroscopy (EIS) was tested at 1.6 V *vs*. RHE for HER or -0.2 V *vs*. RHE for OER in the frequency range from 10 kHz to 10 mHz. All polarization curves were corrected by 90% *i*R-compensation for ohmic losses, including active materials, substrate, and solution resistance. The value of R can be read from the crossing point between the arc and the real axis in the Nyquist plot.

1.3.3 Electrochemical active surface area (ECSA)

To estimate the electrochemical active surface area (ESCA), one important indicator, double layer capacitance (C_{dl}) can be measured from the CV within a narrow potential window where no Faradic process occurs. The currents measured at a certain voltage should be linearly dependent on the active surface area because of the charging capacitance in double layer. For OER half reaction, these CV scans were performed from 1.15 to 1.20 V with different scan rates (2, 4, 6, 8, and 10 mV s^{-1}). The C_{dl} can be determined from the slope of current density (at

1.19 V *vs*. RHE) -overpotential linear curves. For HER, CV scans were performed from 0.03 to 0.23 V with different scan rates (10, 20, 30, 40, and 50 mV s^{-1}).

Supporting Information
Supporting Information is available from the Wiley Online Library or from the author.

Acknowledgements
We acknowledge support from the Innovation and Technology Commission of Hong Kong and the Hong Kong Polytechnic University.

Received: ((will be filled in by the editorial staff))
Revised: ((will be filled in by the editorial staff))
Published online: ((will be filled in by the editorial staff))

References

[1] Z. W. Seh, J. Kibsgaard, C. F. Dickens, I. Chorkendorff, J. K. Nørskov and T. F. Jaramillo, *Science*, **2017**, *355*, 4998.

[2] T. Sheng, Y.-F. Xu, Y.-X. Jiang, L. Huang, N. Tian, Z.-Y. Zhou, I. Broadwell and S.-G. Sun, *Acc. Chem. Res.*, **2016**, *49*, 2569.

[3] L. Zhou, Z. Zhuang, H. Zhao, M. Lin, D. Zhao and L. Mai, *Adv. Mater.*, **2017**, *29*, 1602914.

[4] J. Yin, Y. Li, F. Lv, Q. Fan, Y. Q. Zhao, Q. Zhang, W. Wang, F. Cheng, P. Xi and S. Guo, *ACS Nano*, **2017**, *11*, 2275.

[5] J. Deng, H. Li, S. Wang, D. Ding, M. Chen, C. Liu, Z. Tian, K. S. Novoselov, C. Ma, D. Deng and X. Bao, *Nat. Commun.*, **2017**, *8*, 14430.

[6] H. Liang, A. N. Gandi, D. H. Anjum, X. Wang, U. Schwingenschlögl and H. N. Alshareef, *Nano Lett.*, **2016**, *16*, 7718.

[7] M. Zeng and Y. Li, *J. Mater. Chem. A*, **2015**, *3*, 14942.

[8] I. C. Man, H.-Y. Su, F. Calle-Vallejo, H. A. Hansen, J. I. Martínez, N. G. Inoglu, J. Kitchin, T. F. Jaramillo, J. K. Nørskov and J. Rossmeisl, *ChemCatChem*, **2011**, *3*, 1159.

[9] X. Gao, H. Zhang, Q. Li, X. Yu, Z. Hong, X. Zhang, C. Liang and Z. Lin, *Angew. Chem. Int. Ed.*, **2016**, *55*, 6290.

[10] J. Wang, W. Cui, Q. Liu, Z. Xing, A. M. Asiri and X. Sun, *Adv. Mater.*, **2016**, *28*, 215.

[11] J. Zhang, Y. Hu, D. Liu, Y. Yu and B. Zhang, *Adv. Sci.*, **2017**, *4*, 1600343.

[12] C. Tang, R. Zhang, W. Lu, L. He, X. Jiang, A. M. Asiri, and X. Sun, *Adv. Mater.,* **2017**, *29*, 1602441.

[13] X. Ji, R. Zhang, X. Shi, A. M. Asiri, B. Zheng and X. Sun, *Nanoscale,* **2018**, *10*, 7941.

[14] B. S. Yeo and A. T. Bell, *J. Am. Chem. Soc.*, **2011**, *133*, 5587.

[15] M. Ledendecker, G. Clavel, M. Antonietti and M. Shalom, *Adv. Funct. Mater.*, **2015**, *25*, 393.

[16] H. Furukawa, K. E. Cordova, M. O'Keeffe and O. M. Yaghi, *Science*, **2013**, *341*, 1230444.

[17] K. Manna, P. Ji, Z. Lin, F. X. Greene, A. Urban, N. C. Thacker and W. Lin, *Nat. Commun.*, **2016**, *7*, 12610.

[18] M.-S. Yao, X.-J. Lv, Z.-H. Fu, W.-H. Li, W.-H. Deng, G.-D. Wu, and G. Xu, *Angew. Chem. Int. Ed.,* **2017**, *56*, 16510.

[19] K. Tan, S. Zuluaga, Q. Gong, P. Canepa, H. Wang, J. Li, Y. J. Chabal and T. Thonhauser, *Chem. Mater.*, **2014**, *26*, 6886.

[20] W.-H. Li, K. Ding, H.-R. Tian, M.-S. Yao, B. Nath, W.-H. Deng, Y. Wang and G. Xu, *Adv. Funct. Mater.*, **2017**, *27*, 1702067.

[21] Z. F. Huang, J. Song, K. Li, M. Tahir, Y. T. Wang, L. Pan, L. Wang, X. Zhang and J. J. Zou, *J. Am. Chem. Soc.*, **2016**, *138*, 1359.

[22] T. Y. Ma, S. Dai, M. Jaroniec and S. Z. Qiao, *J. Am. Chem. Soc.*, **2014**, *136*, 13925.

[23] X.-F. Lu, L.-F. Gu, J.-W. Wang, J.-X. Wu, P.-Q. Liao and G.-R. Li, *Adv. Mater.*, **2017**, *29*, 1604437.

[24] S. Huang, Y. Meng, S. He, A. Goswami, Q. Wu, J. Li, S. Tong, T. Asefa and M. Wu, *Adv. Funct. Mater.*, **2017**, *27*, 1606585.

[25] X. Cao, C. Tan, M. Sindoro and H. Zhang, *Chem. Soc. Rev.*, **2017**, *46*, 2660.

[26] Y. Hou, T. Huang, Z. Wen, S. Mao, S. Cui and J. Chen, *Adv. Energy Mater.*, **2014**, *4*, 1400337.

[27] J. Zhou, Y. Dou, A. Zhou, R.-M. Guo, M.-J. Zhao and J.-R. Li, *Adv. Energy Mater.*, **2017**, *7*, 1602643.

[28] J.-S. Qin, D.-Y. Du, W. Guan, X.-J. Bo, Y.-F. Li, L.-P. Guo, Z.-M. Su, Y.-Y. Wang, Y.-Q. Lan and H.-C. Zhou, *J. Am. Chem. Soc.*, **2015**, *137*, 7169.

[29] B. Nohra, H. El Moll, L. M. Rodriguez Albelo, P. Mialane, J. Marrot, C. Mellot-Draznieks, M. O'Keeffe, R. Ngo Biboum, J. Lemaire, B. Keita, L. Nadjo and A. Dolbecq, *J. Am. Chem. Soc.*, **2011**, *133*, 13363.

[30] J. Duan, S. Chen and C. Zhao, *Nat. Commun.*, **2017**, *8*, 15341.

[31] S. Zhao, Y. Wang, J. Dong, C.-T. He, H. Yin, P. An, K. Zhao, X. Zhang, C. Gao, L. Zhang, J. Lv, J. Wang, J. Zhang, A. M. Khattak, N. A. Khan, Z. Wei, J. Zhang, S. Liu, H. Zhao and Z. Tang, *Nat. Energy*, **2016**, *1*, 16184.

[32] C. Guan, X. Liu, W. Ren, X. Li, C. Cheng and J. Wang, *Adv. Energy Mater.*, **2017**, *7*, 1602391.

[33] M. Zhao, Y. Wang, Q. Ma, Y. Huang, X. Zhang, J. Ping, Z. Zhang, Q. Lu, Y. Yu, H. Xu, Y. Zhao and H. Zhang, *Adv. Mater.*, **2015**, *27*, 7372.

[34] Q. Liu, L. Xie, X. Shi, G. Du, A. M. Asiri, Y. Luo and X. Sun, *Inorg. Chem. Front.,* **2018**, *5*, 1570

[35] X. Zhang, Q. Liu, X. Shi, A. M. Asiri and X. Sun, *Inorg. Chem. Front.,* **2018**, *5*, 1405.

[36] K. Zhao, S. Liu, G. Ye, Q. Gan, Z. Zhou and Z. He, *J. Mater. Chem. A*, **2018**, *6*, 2166.

[37] G. S. Papaefstathiou, T. Friscić and L. R. MacGillivray, *J. Am. Chem. Soc.*, **2005**, *127*, 14160.

[38] J. Huang, Y. Li, R. K. Huang, C. T. He, L. Gong, Q. Hu, L. Wang, Y. T. Xu, X. Y. Tian, S. Y. Liu, Z. M. Ye, F. Wang, D. D. Zhou, W. X. Zhang and J. P. Zhang, *Angew. Chem. Int. Ed.*, **2018**, *57*, 4632.

[39] J. Yang, P. Xiong, C. Zheng, H. Qiu and M. Wei, *J. Mater. Chem. A*, **2014**, *2*, 16640.

[40] J. A. Kaduk and J. A. Hanko, *J. Appl. Crystallogr.*, **2001**, *34*, 710.

[41] A. Mineshige, M. Inaba, T. Yao, Z. Ogumi, K. Kikuchi, M. Kawase, *J. Solid State Chem.,* **1996**, *121*, 423-429

[42] A. Sivanantham, P. Ganesan and S. Shanmugam, *Adv. Funct. Mater.*, **2016**, *26*, 4661.

[43] Y. Jiao, J. Pei, D. Chen, C. Yan, Y. Hu, Q. Zhang and G. Chen, *J. Mater. Chem. A*, **2017**, *5*, 1094.

[44] Y. Ma, Z. He, Z. Wu, B. Zhang, Y. Zhang, S. Ding and C. Xiao, *J. Mater. Chem. A*, **2017**, *5*, 24850.

[45] D. Manova, D. Hirsch, J. W. Gerlach, S. Mändl, H. Neumann and B. Rauschenbach, *Surf. Coat. Technol.*, **2014**, *259*, 434.

[46] B. You, X. Liu, G. Hu, S. Gul, J. Yano, D. E. Jiang and Y. Sun, *J. Am. Chem. Soc.*, **2017**, *139*, 12283.

[47] X. Jia, Y. Zhao, G. Chen, L. Shang, R. Shi, X. Kang, G. I. N. Waterhouse, L. Z. Wu, C. H. Tung and T. Zhang, *Adv. Energy Mater.*, **2016**, *6*, 1.

[48] B. Zhang, C. Xiao, S. Xie, J. Liang, X. Chen and Y. Tang, *Chem. Mater.*, **2016**, *28*, 6934.

[49] L. Han, K. Feng and Z. Chen, *Energy Technol.*, **2017**, *5*, 1908.

[50] J. Zhou, Y. Dou, A. Zhou, R. M. Guo, M. J. Zhao and J. R. Li, *Adv. Energy Mater.*, **2017**, *7*, 1602643.

[51] D. R. Deng, F. Xue, Y. J. Jia, J. C. Ye, C. D. Bai, M. S. Zheng and Q. F. Dong, *ACS Nano*, **2017**, *11*, 6031.

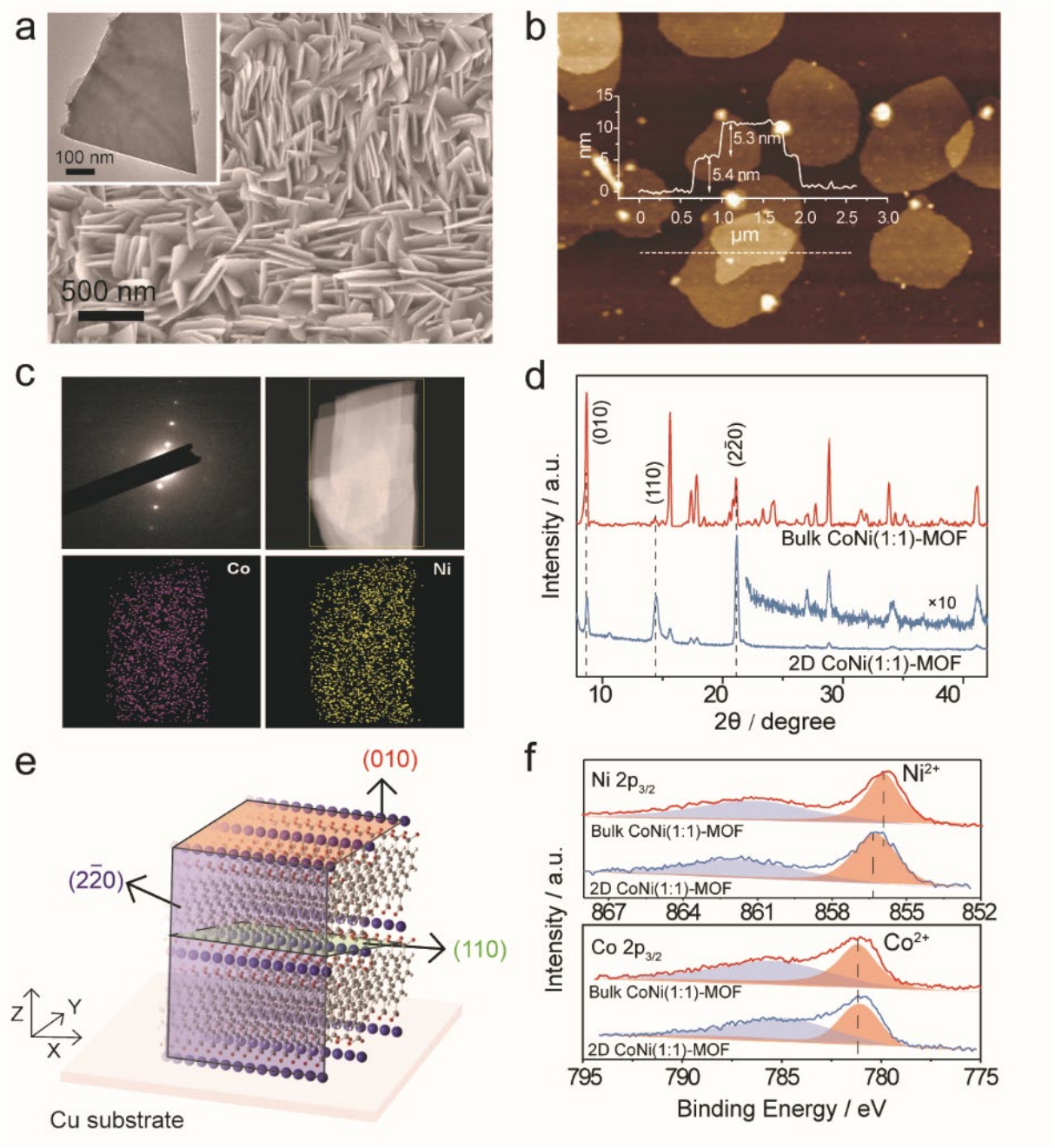

Figure 1. (a) SEM image of 2D CoNi(1:1)-MOF on Cu substrate. Inset is the TEM image of a single nanoplate; (b) AFM image of nanoplates from CoNi(1:1)-MOF and the corresponding cross-sectional analysis; (c) SAED pattern and Co and Ni elemental distribution mapping of 2D CoNi(1:1)-MOF; (d) XRD patterns of 3D and 2D CoNi(1:1)-MOFs; (e) Illustration of 2D M (M = Co, Ni)-MOF on Cu substrate. (2$\bar{2}$0), (110), and (010) facets are shown. Metal ions are shown in blue, oxygen in red, and carbon in grey; (f) XPS spectra (Ni $2p_{3/2}$ and Co $2p_{3/2}$) of 3D and 2D CoNi(1:1)-MOFs.

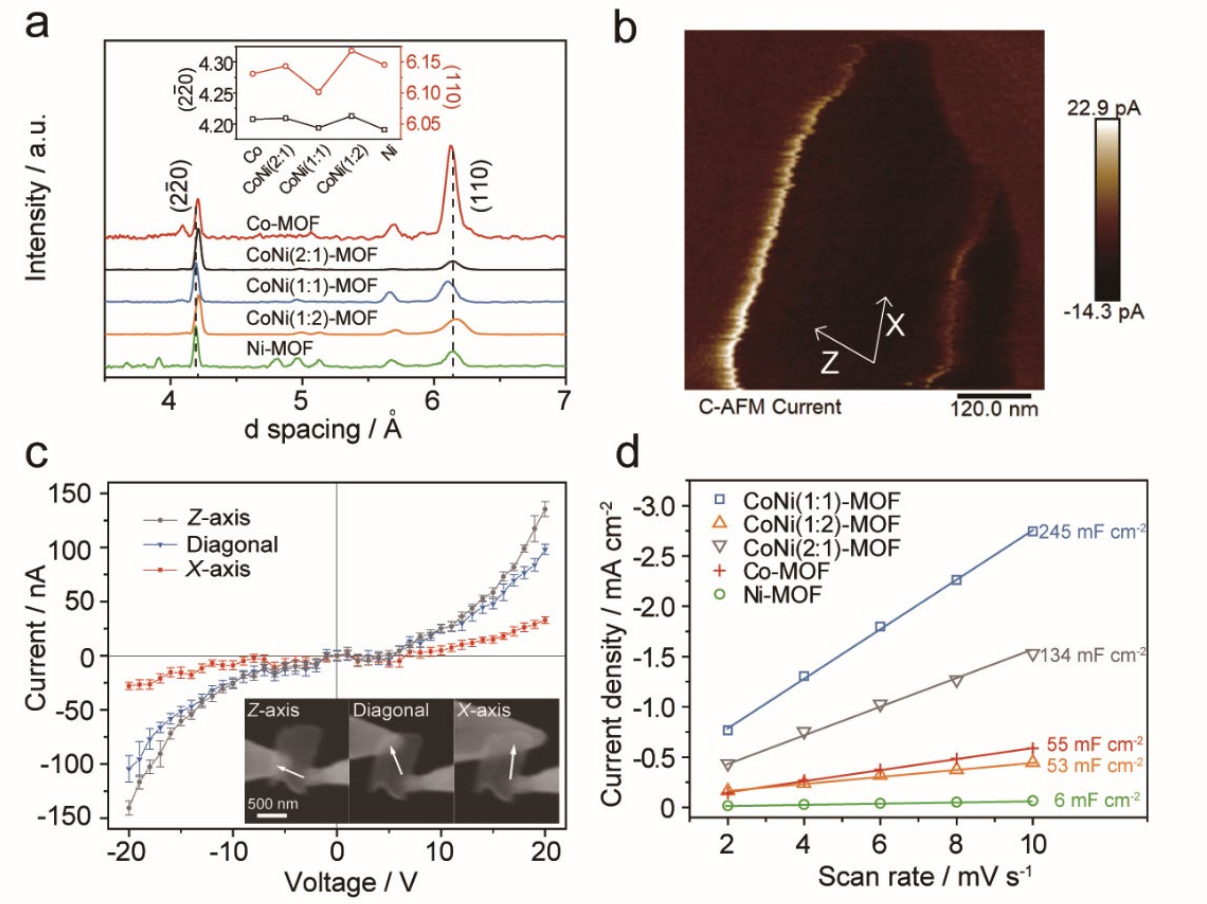

Figure 2. (a) XRD patterns of Co-, Ni-, and CoNi-MOF. Inset shows the *d*-spacings of (2$\bar{2}$0) and (110) facets; (b) *In situ* conducting-AFM image of a CoNi(1:1)-MOF nanoplate on Cu substrate, which was operated under the constant drive amplitude of 100 mV; (c) *i*-V curves of three directions. Insets are SEM images of a CoNi(1:1)-MOF nanoplate with different contact positions; The arrows indicate the *Z*-axis, diagonal, and *X*-axis direction of connection; (d) Areal capacitance characterization of MOFs in 1 M KOH using CVs.

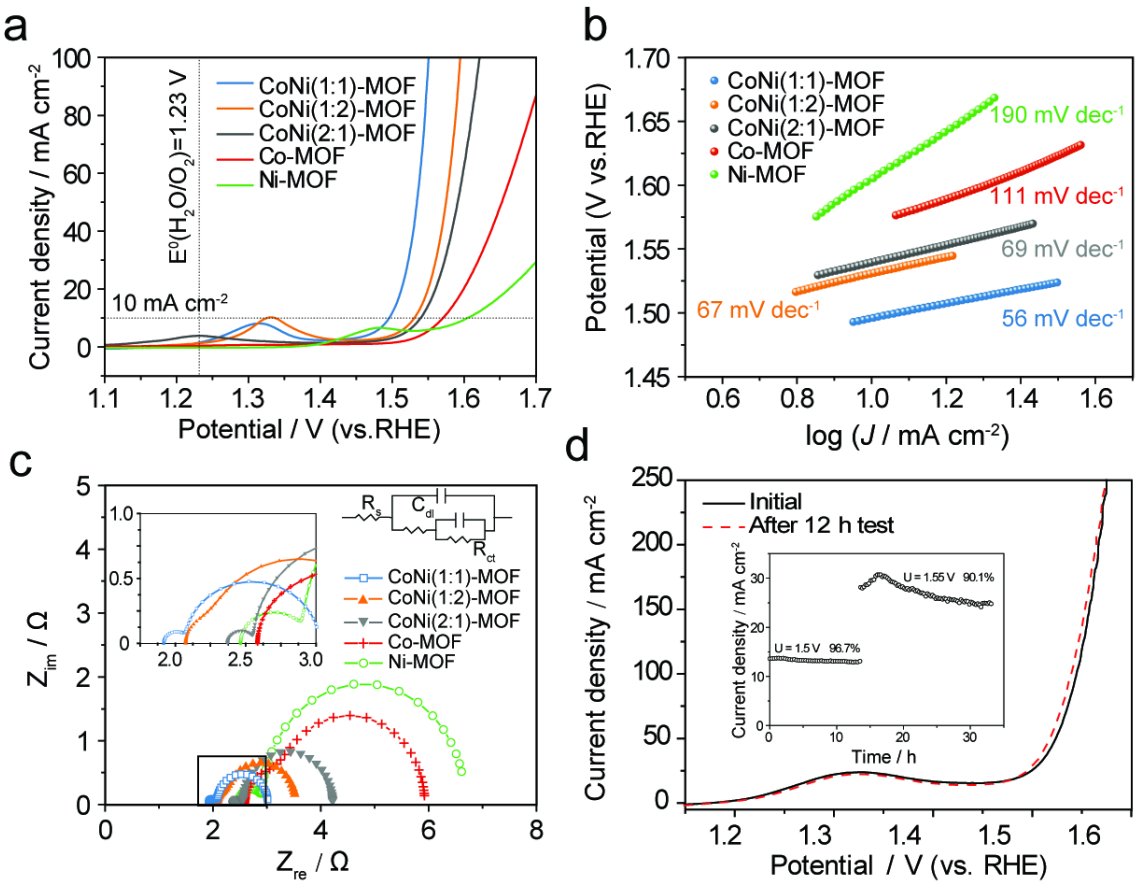

Figure 3. (a) Linear polarization curves of OER reaction in 1 M KOH using MOFs as electrocatalyst with 90% *i*R-correction; (b) Tafel plots converted from polarization curves; (c) EIS plots recorded at 1.55 V *vs*. RHE. Inset shows the high-frequency range (left) and the equivalent circuit (right); (d) The polarization curves before and after 12-hour electrolysis using CoNi(1:1)-MOF as electrocatalyst with the scan rate of 10 mV/s without *i*R-correction. Inset is long-term stability test carried out at 1.5 V and 1.55 V, respectively.

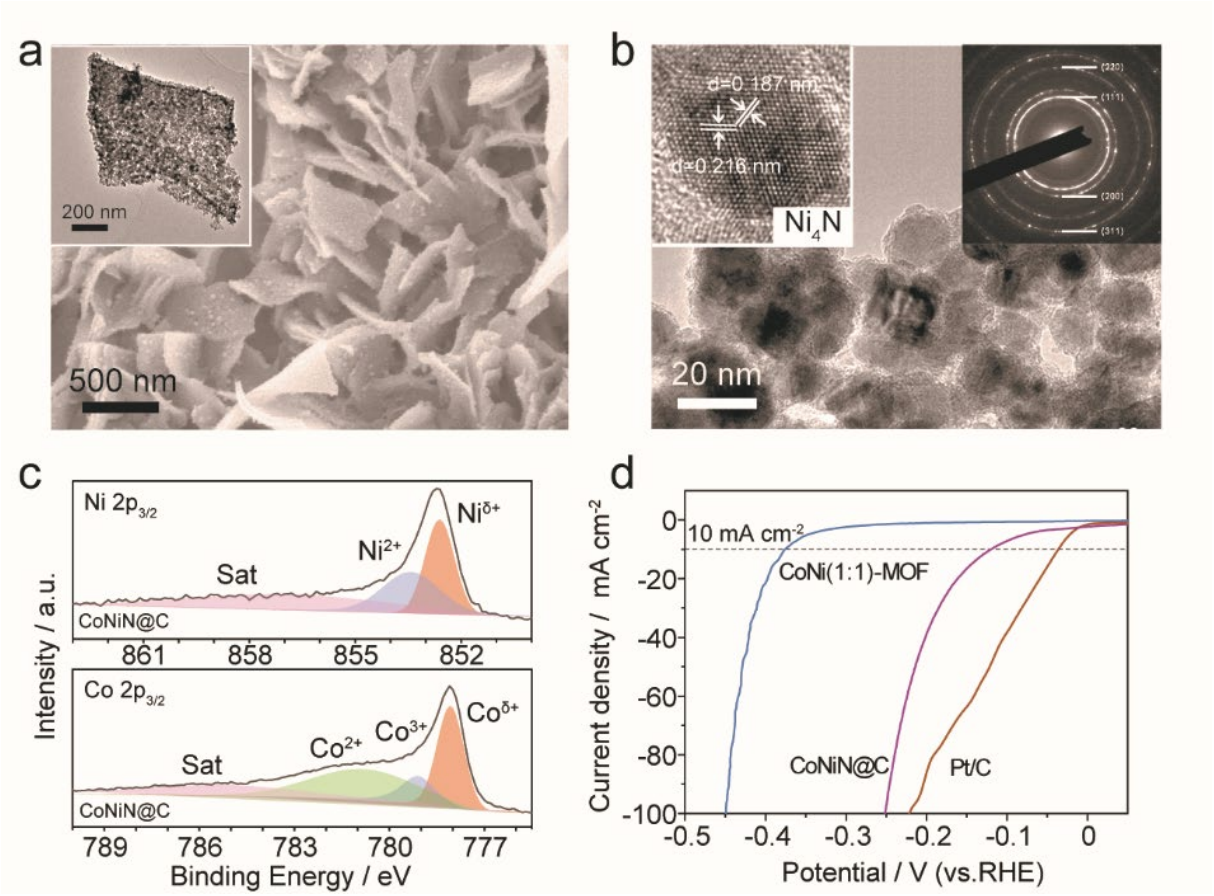

Figure 4. (a) SEM image of 2D CoNiN@C. Inset is the TEM image of a nanoplate; (b) HRTEM image of CoNiN@C. Insets show the lattice fringes of Ni_4N (left) and the corresponding SAED pattern (right); (c) XPS spectra of Ni $2p_{3/2}$ and Co $2p_{3/2}$ of CoNiN@C; (d) Linear polarization curves of HER reaction in 1 M KOH using CoNiN@C, CoNi(1:1)-MOF, and Pt/C as electrocatalyst with 90% *i*R-correction.

2D bimetallic CoNi(1:1)-MOF with the (2$\bar{2}$0) crystalline facets exposed catalyzes oxygen evolution at a low overpotential of 265 mV. CoNiN@C prepared using CoNi-MOF as a precursor shows comparable hydrogen evolution rate in alkaline solution. Using CoNi(1:1)-MOF and CoNiN@C, overall water splitting was achieved with 99.0% (HER) and 98.9% (OER) Faradaic efficiencies.

Keywords:
Water splitting, bimetallic MOF, 2D MOF, nanoplate array, electrocatalyst

Authors:
Mengjie Liu, Weiran Zheng, Sijia Ran, Steven T. Boles, and Lawrence Yoon Suk Lee*

Overall Water Splitting Electrocatalysts by 2D CoNi Metal-Organic Framework and its Derivative

ToC figure

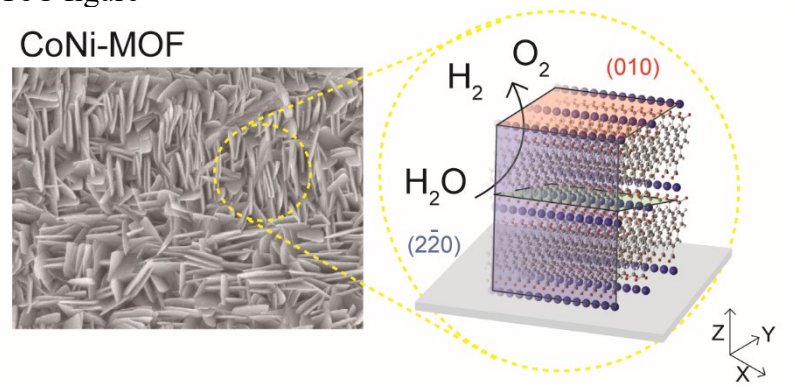

Supporting Information

Overall Water Splitting Electrocatalysts based on 2D CoNi Metal-Organic Frameworks and Its Derivative

*Mengjie Liu, Weiran Zheng, Sijia Ran, Steven T. Boles, and Lawrence Yoon Suk Lee**

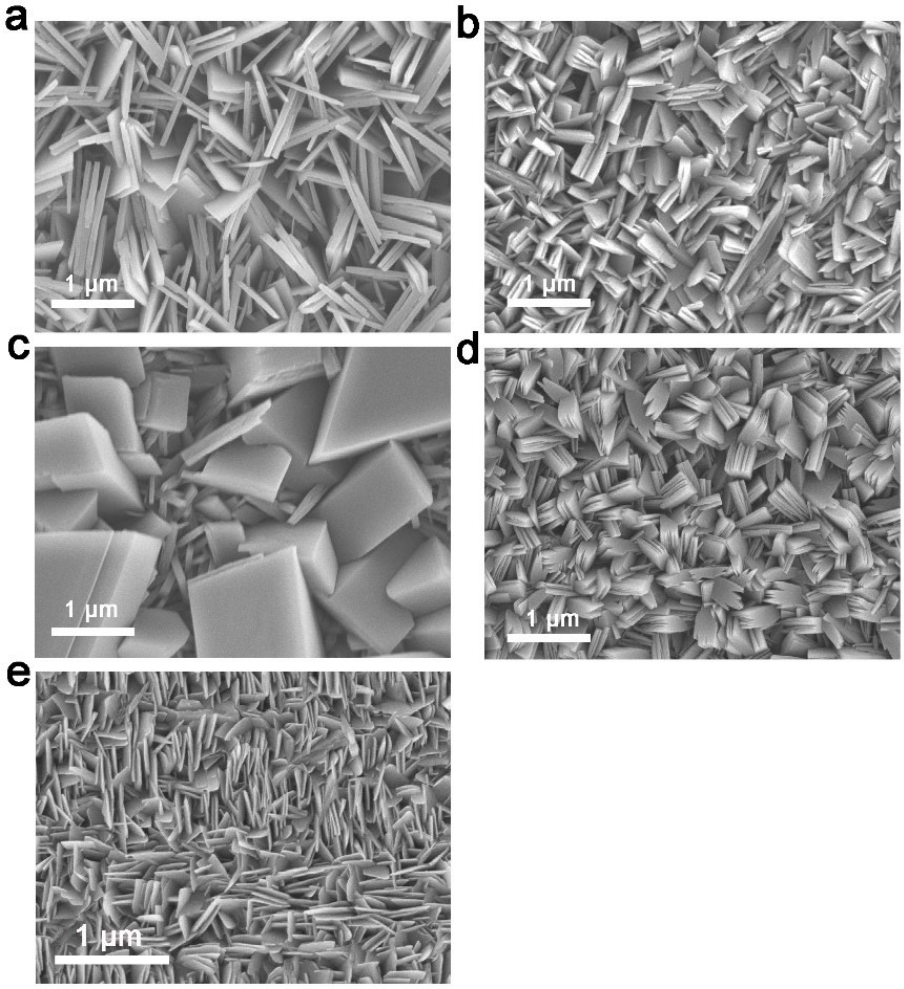

Figure S1. SEM images of the CoNi-MOFs prepared with different Co and Ni precursor ratios. a) CoNi(1:2)-, b) CoNi(2:1)-, c) Ni-, d) Co-, and e) CoNi(1:1)-MOF.

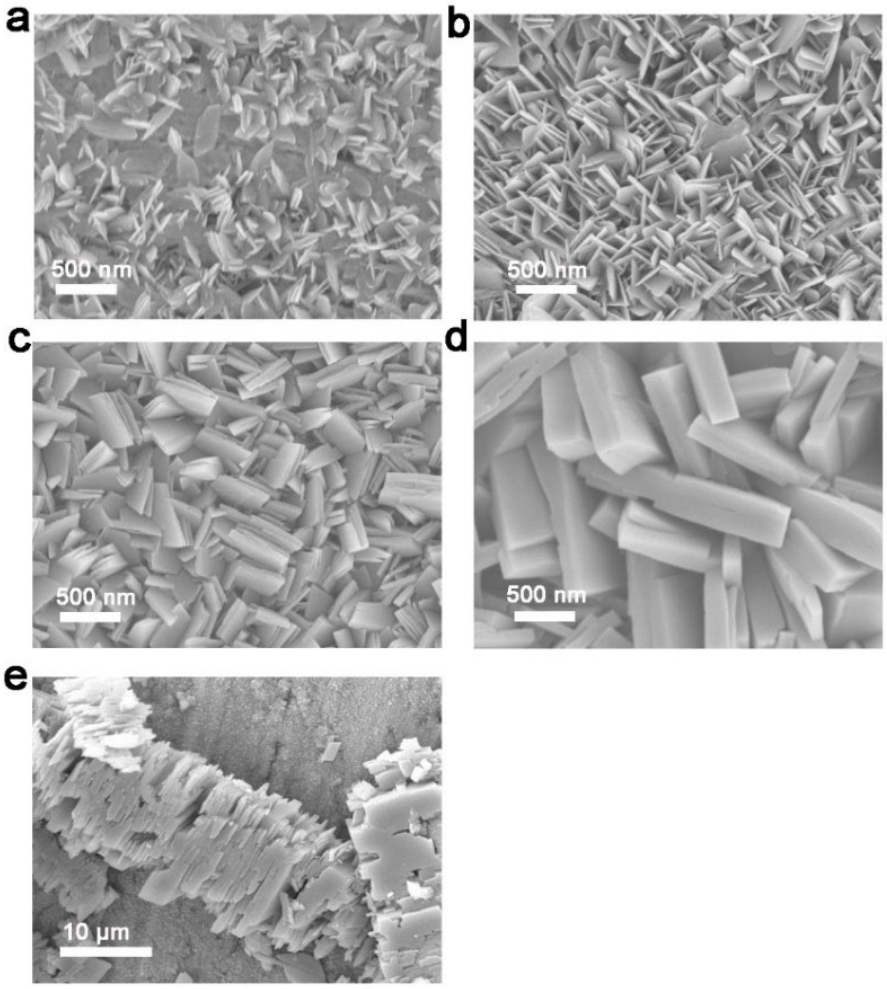

Figure S2. SEM images of CoNi(1:1)-MOF prepared with different reaction times. a) 0.5 h, b) 2 h, c) 6 h, d) 10 h and e) 3D bulk CoNi(1:1)-MOF grown without Cu substrate.

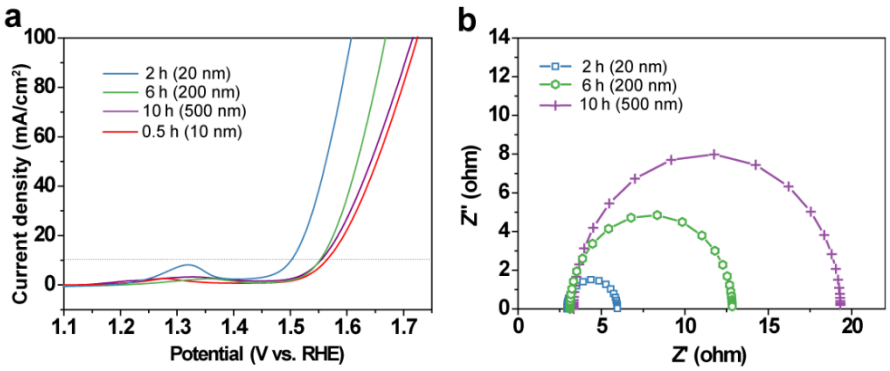

Figure S3. (a) Linear polarization curves and (b) EIS plots of OER reaction in 1 M KOH without *i*R-correction using MOFs with different thicknesses

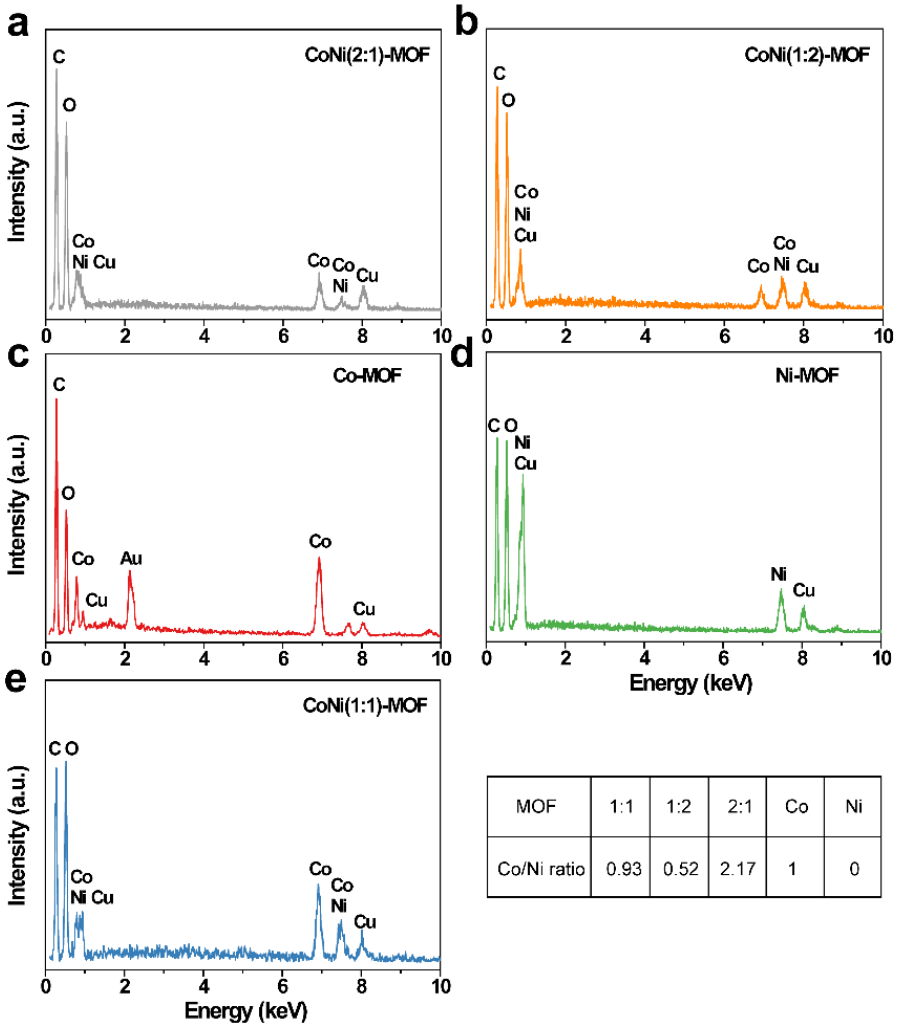

MOF	1:1	1:2	2:1	Co	Ni
Co/Ni ratio	0.93	0.52	2.17	1	0

Figure S4. EDS and corresponding elemental compositions of the CoNi-MOFs with different metal ratios.

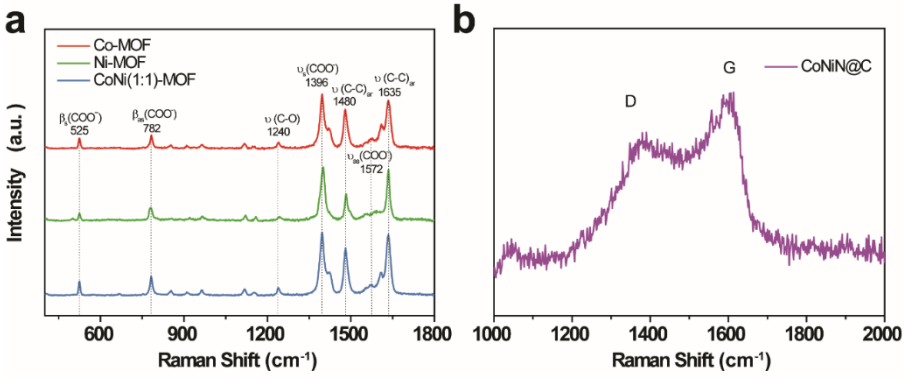

Figure S5. Raman spectra of (a) Co-, Ni-, and CoNi(1:1)-MOFs and (b) CoNiN@C.

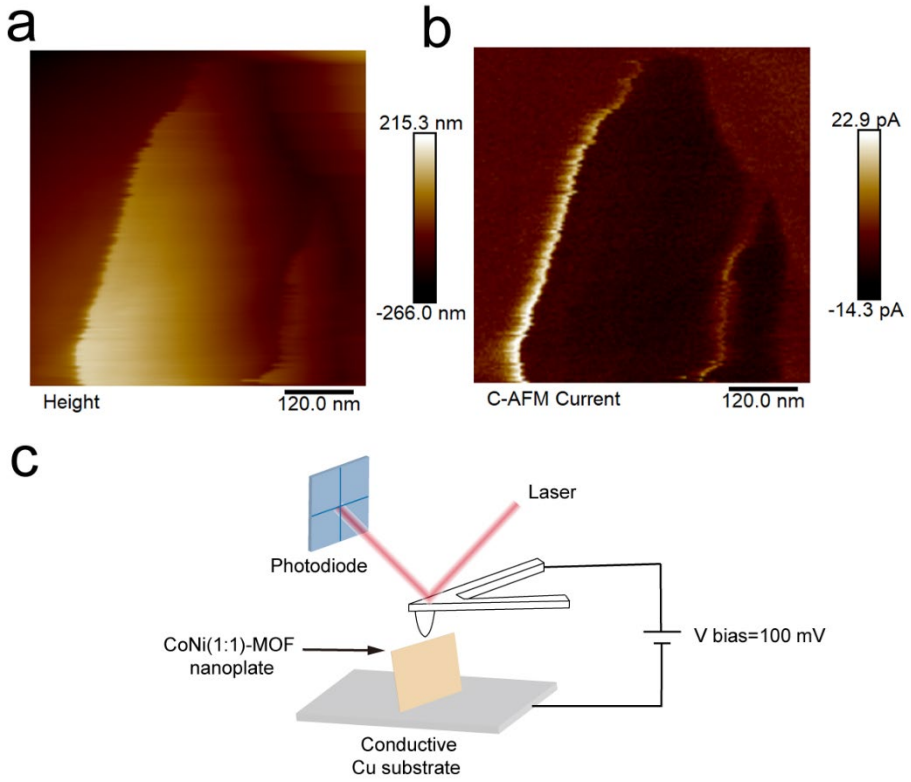

Figure S6. (a) Topological AFM image, (b) conducting-AFM image of two CoNi(1:1)-MOF nanoplates on Cu substrate, and (c) the schematics of conductive-AFM experiment.

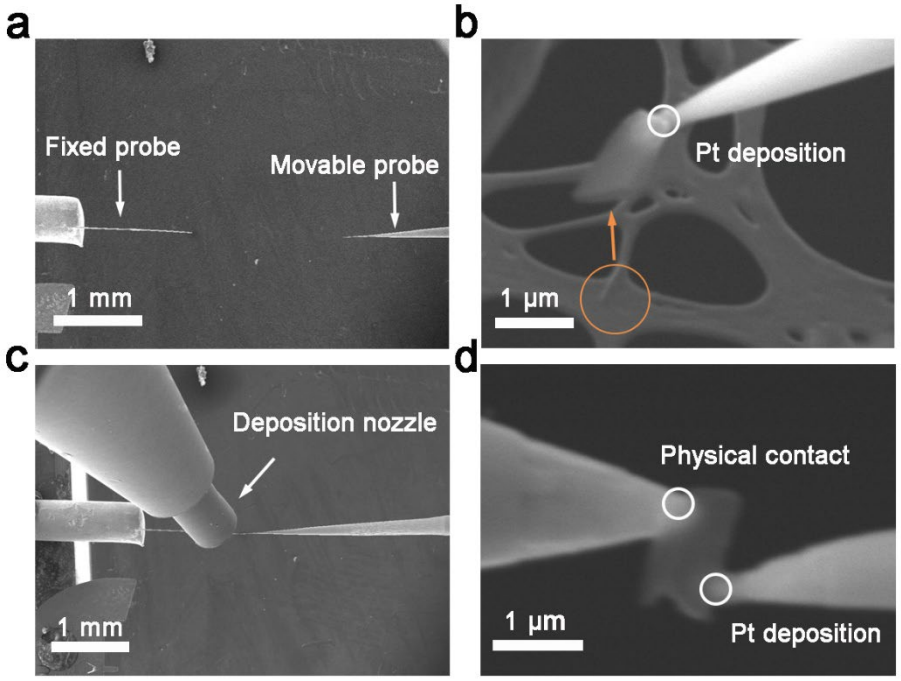

Figure S7. The setup and measuring process of FIB. (a) Two conductive probes for connecting sample, (b) the harvesting of sample from carbon membrane, (c) Pt deposition nozzle, and (d) the successful contact between two probes and sample.

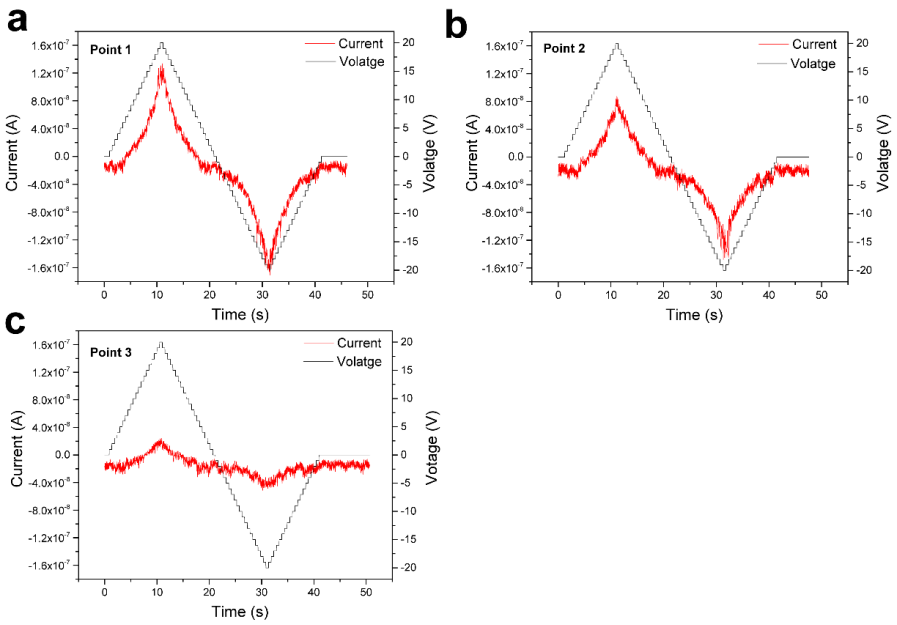

Figure S8. The voltage sweepings and the corresponding current response curves of a) Point 1: *Z* direction, b) point 2: diagonal, and c) point 3: *X* direction. Voltage ranges from -20 to 20 V, 1 V per step, 0.5 s time interval, 40 Hz acquisition rate.

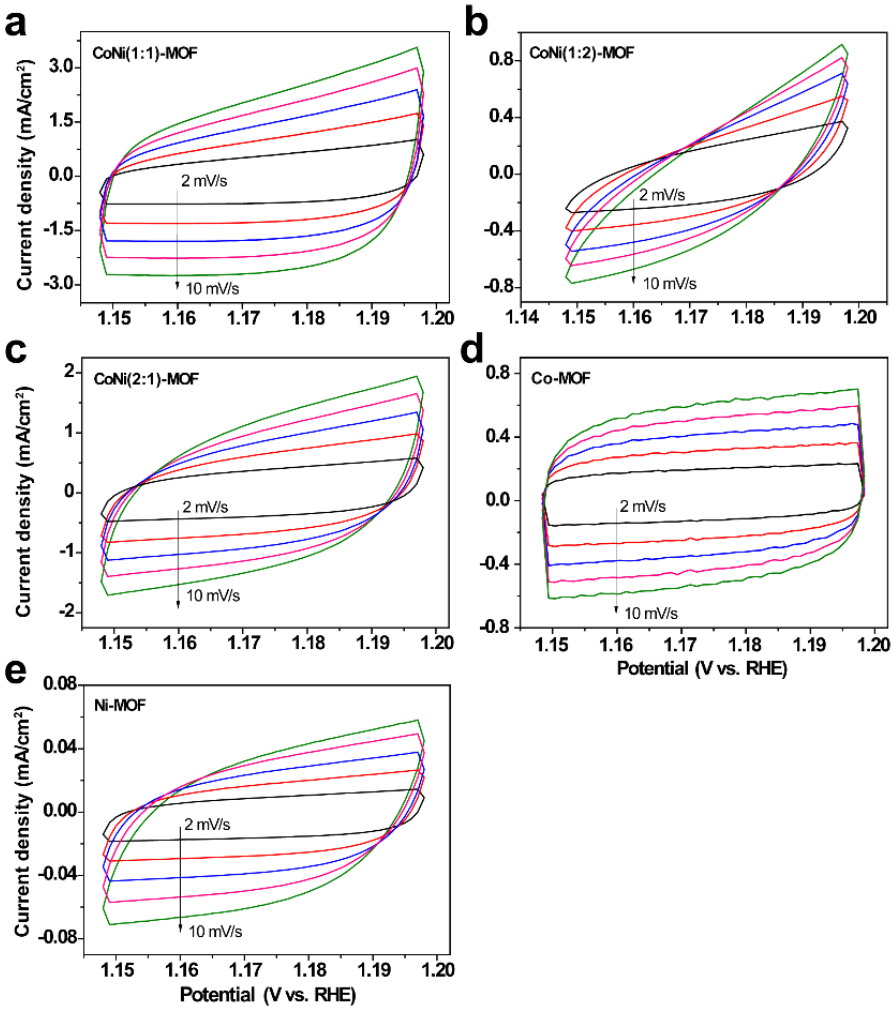

Figure S9. Cyclic voltammograms of (a) CoNi(1:1)-, (b) CoNi(1:2)-, (c) CoNi(2:1)-, (d) Co-MOF, and (e) Ni-MOF measured at different scan rates from 2 to 10 mV/s.

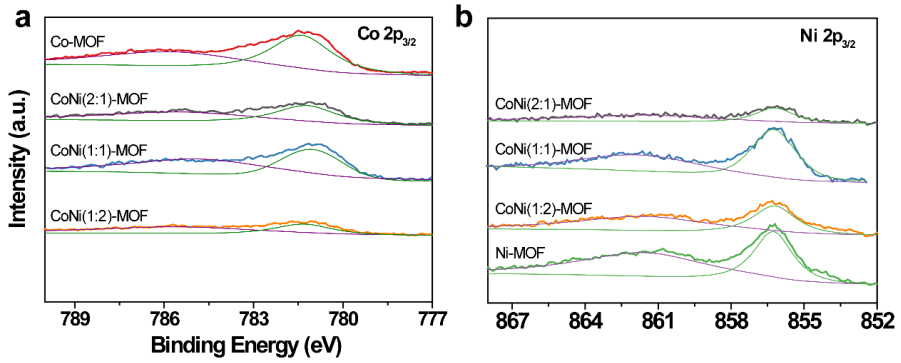

Figure S10. (a) Co $2p_{3/2}$ and (b) Ni $2p_{3/2}$ XPS spectra of Co-, CoNi(2:1)-, CoNi(1:1)-, CoNi(1:2)-, and N-MOFs

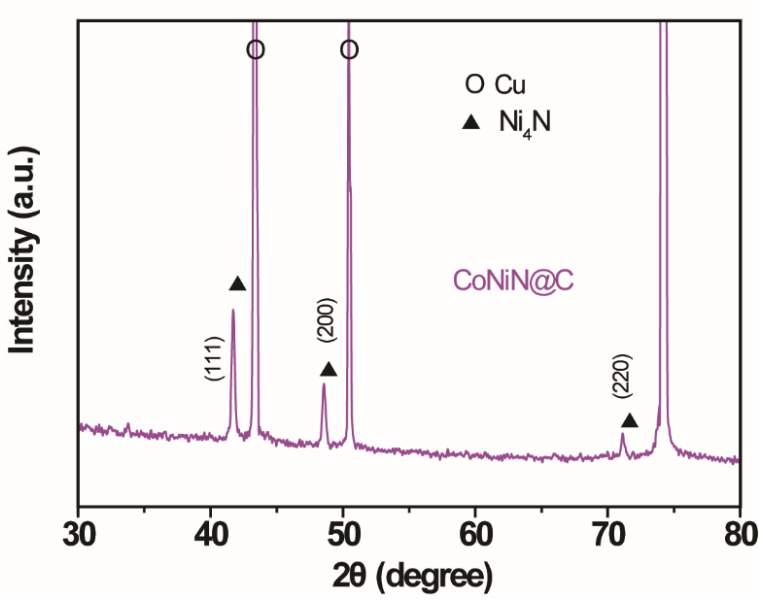

Figure S11. XRD pattern of CoNiN@C.

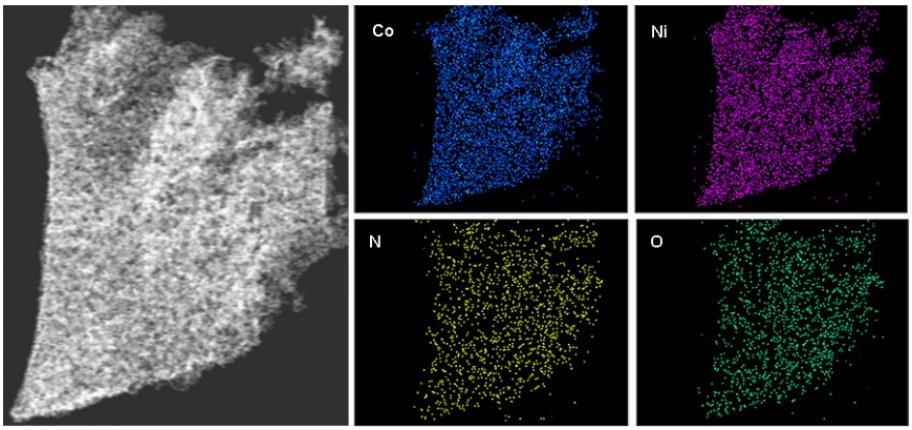

Figure S12. Elemental distribution mapping of CoNiN@C.

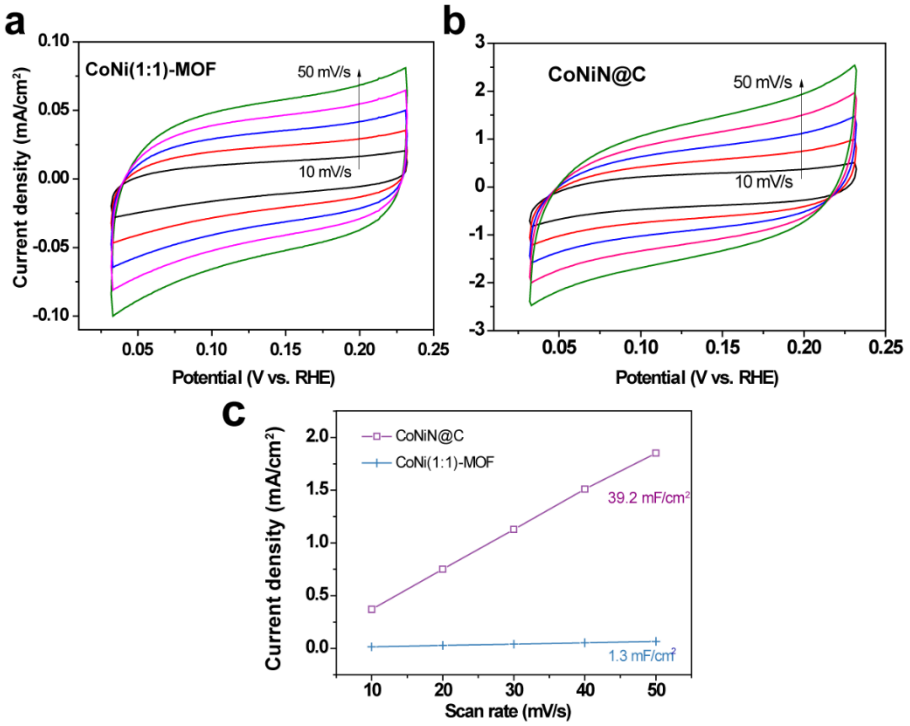

Figure S13. Cyclic voltammograms of (a) CoNi(1:1)-MOF and (b) CoNiN@C measured at different scan rates from 10 to 50 mV/s, and (c) the plot of capacitance against scan rate for calculating areal capacities of CoNi(1:1)-MOF and CoNiN@C.

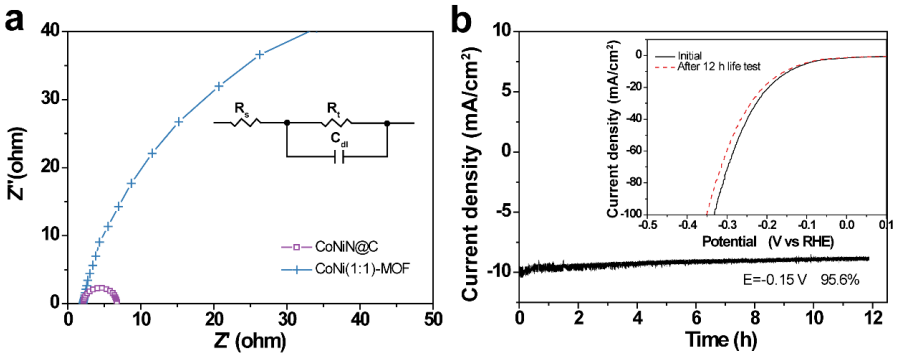

Figure S14. (a) EIS plots of CoNiN@C and CoNi(1:1)-MOF recorded at -0.25 V *vs*. RHE. Inset shows the equivalent circuit; (b) Long-term stability test carried out at -0.15 V using CoNiN@C as a HER electrocatalyst. Inset shows the polarization curves before and after a 12 h test.

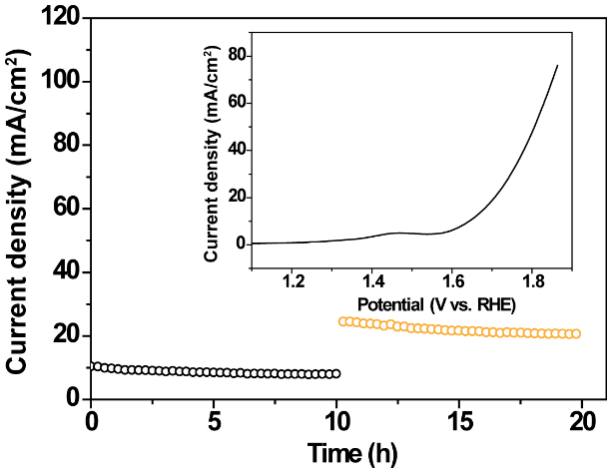

Figure S15. Long-term stability test carried out at 1.64 and 1.70 V using CoNi(1:1)-MOF as an anode and CoNiN@C as a cathode, respectively, for the overall water splitting. Inset shows 90% *i*R-corrected polarization curve.

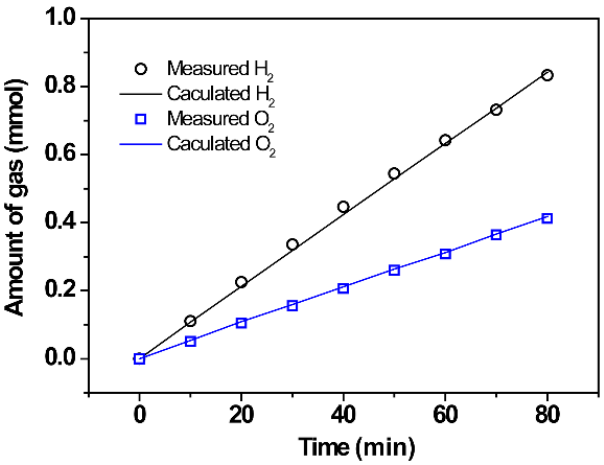

Figure S16. The amount of H_2 and O_2 calculated and measured plotted against the overall water splitting reaction time for CoNi(1:1)-MOF‖CoNiN@C. The current density is 15 mA/cm^2 for 80 min.

Taking the amount of O_2 generated in 80 min reaction as an example:

$$\text{Faraday Effiency}(\%) = \frac{Q_{O_2}}{Q_{practically}} = \frac{n_{O_2} \times z \times F}{Q_{pratically}}$$

$$= \frac{4.125 \times 10^{-4}\ mol \times 4 \times 96{,}485\ C/mol}{1.614 \times 10^{2}\ C} = 99.0\%$$

Take the amount of generated H_2 within 80 mins as the example:

$$\text{Faraday Effiency}(\%) = \frac{Q_{H_2}}{Q_{practically}} = \frac{n_{H_2} \times z \times F}{Q_{pratically}}$$

$$= \frac{8.333 \times 10^{-4}\ mol \times 2 \times 96{,}485\ C/mol}{1.625 \times 10^{2}\ C} = 98.9\%$$

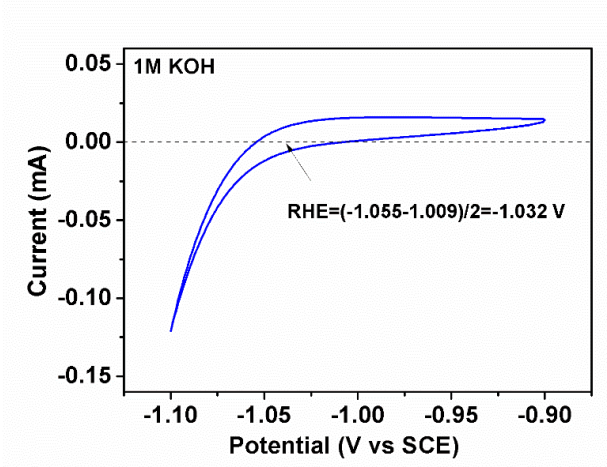

Figure S17. The CV curve of SCE in H_2-saturated 1 M KOH for the calibration of potential values measured against SCE to RHE.

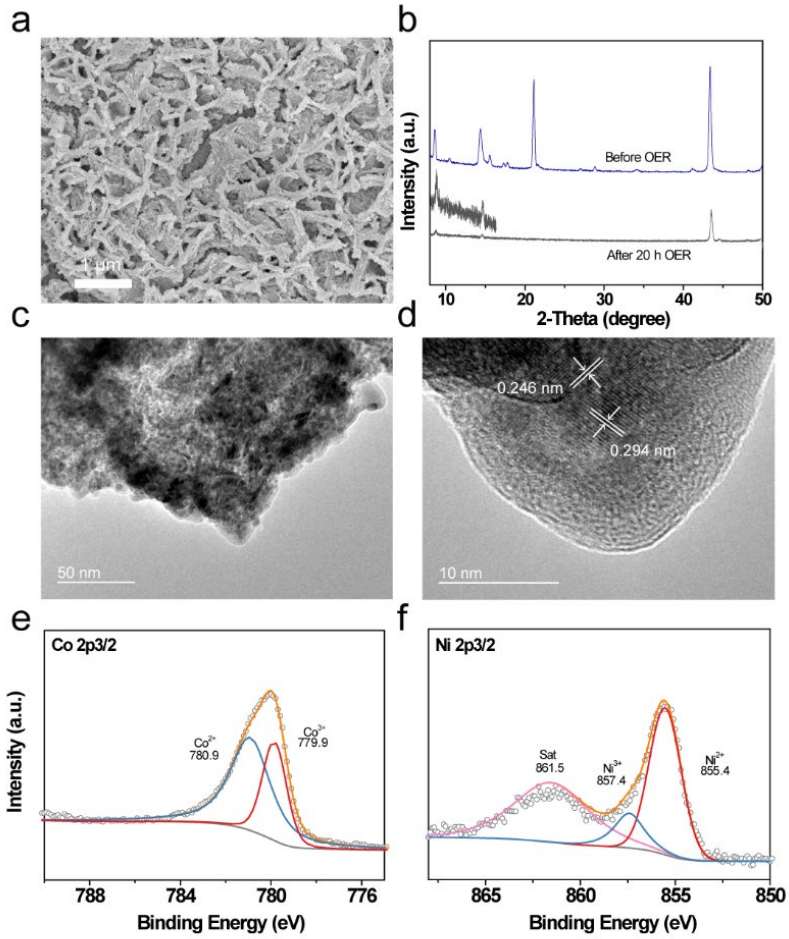

Figure S18. (a) SEM; (b) XRD; (c,d) TEM; and (e,f) XPS characterization after 20 h OER reaction in 1 M KOH.

Table S1. Summary of the OER performance of CoNi(1:1)-MOF and other reported catalysts.

Sample	**Substrate**	**Overpotential (at 10 mA/cm^2)**	**Tafel slope**	**Electrolyte**	**Reference**
CoNi(1:1)-MOF	Cu foil	265	56	1 M KOH	**This work**
NiCoP	Ni foam	280	87	1 M KOH	[1]
Co_3O_4-carbon	Cu foil	290	70	0.1 M KOH	[2]
NiCo-UMOFNs	/	250	42	1 M KOH	[3]
Co_3O_4@CoP	Ni foil	238	52	1 M KOH	[4]
$NiCo_2O_4$ Hollow	Ni foam	290	53	1 M NaOH	[5]
Co_9S_8@NOSC	GCE	340	68	1 M KOH	[6]
NiFe-MOF	Ni foam	240	34	0.1M KOH	[7]
Ni/NiP	Ni foam	270	73.2	1 M KOH	[8]
$NiCo_2S_4$ NW/NF	Ni foam	260	40.1	1 M KOH	[9]

* UMOFNs = ultrathin metal-organic framework nanosheets; Co_9S_8@NOSC = N-, O-, and S-tridoped carbon-encapsulated Co_9S_8; NW = nanowire; NF = nickel foam

Table S2. Summary of the HER performance of CoNiN@C and other reported catalysts.

Sample	Substrate	Overpotential (at 10	Tafel slope	Electrolyte	Reference
CoNiN@C	Cu foil	120	140	1 M KOH	**This work**
NiCoP	Ni foam	32	47.9	1 M KOH	[1]
$NiCo_2O_4$ Hollow Microcuboids	Ni foam	110	47.9	1 M NaOH	[5]
Co_9S_8@NOSC	GCE	320	105	1 M KOH	[6]
NiFe-MOF	Ni foam	134	42	1 M KOH	[7]
Ni/NiP	Ni foam	130	58.5	1 M KOH	[8]
$NiCo_2S_4$	Ni foam	210	58.9	1 M KOH	[9]

* Co_9S_8@NOSC = N-, O-, and S-tridoped carbon-encapsulated Co_9S_8; NW = nanowire; NF = nickel foam

References

1 H. Liang, A. N. Gandi, D. H. Anjum, X. Wang, U. Schwingenschlögl and H. N. Alshareef, *Nano Lett.*, 2016, **16**, 7718–7725.

2 T. Y. Ma, S. Dai, M. Jaroniec and S. Z. Qiao, *J. Am. Chem. Soc.*, 2014, **136**
, 13925–13931.

3 S. Zhao, Y. Wang, J. Dong, C.-T. He, H. Yin, P. An, K. Zhao, X. Zhang, C. Gao, L. Zhang, J. Lv, J. Wang, J. Zhang, A. M. Khattak, N. A. Khan, Z. Wei, J. Zhang, S. Liu, H. Zhao and Z. Tang, *Nat. Energy*, 2016, **1**, 16184–16194.

4 J. Zhou, Y. Dou, A. Zhou, R. M. Guo, M. J. Zhao and J. R. Li, *Adv. Energy Mater.*, 2017, **7**, 1602643–1602653.

5 X. Gao, H. Zhang, Q. Li, X. Yu, Z. Hong, X. Zhang, C. Liang and Z. Lin, *Angew. Chem., Int. Ed.*, 2016, **55**, 6290–6294.

6 S. Huang, Y. Meng, S. He, A. Goswami, Q. Wu, J. Li, S. Tong, T. Asefa and M. Wu, *Adv. Funct. Mater.*, 2017, **27**, 1606585–1606595.

7 J. Duan, S. Chen and C. Zhao, *Nat. Commun.*, 2017, **8**, 15341–15348.

8 G.-F. Chen, T. Y. Ma, Z.-Q. Liu, N. Li, Y.-Z. Su, K. Davey and S.-Z. Qiao, *Adv. Funct. Mater.*, 2016, **26**, 3314–3323.

9 A. Sivanantham, P. Ganesan and S. Shanmugam, *Adv. Funct. Mater.*, 2016, **26**, 4661–4672.